Flow, Turbulence and Combustion **66:** 427–451, 2001.

'T-RANS' Simulation of Deterministic Eddy Structure in Flows Driven by Thermal Buoyancy and Lorentz Force

K. HANJALIĆ and S. KENJEREŠ
Thermofluids Section, Department of Applied Physics, Delft University of Technology, Lorentzweg 1, 2628 CJ Delft, The Netherlands; E-mail: hanjalic@ws.tn.tudelft.nl

Received 25 May 2000; accepted in revised form 14 May 2001

Abstract. The paper reports on the application of the Time-dependent Reynolds-Averaged Navier–Stokes (T-RANS) approach to analysing the effects of magnetic force and bottom-wall configuration on the reorganisation of a large coherent structure and its role in the transport processes in Rayleigh–Bénard convection. The large-scale deterministic motion is fully resolved in time and space, whereas the unresolved stochastic motion is modelled by a 'subscale' model for which the conventional algebraic stress/flux expressions were used, closed with the low-Re number $\langle k\rangle$-$\langle\varepsilon\rangle$-$\langle\theta^2\rangle$ three-equation model. The applied method reproduces long-term averaged mean flow properties, turbulence second moments, and all major features of the coherent roll/cell structure in classic Rayleigh–Bénard convection in excellent agreement with the available DNS and experimental results. Application of the T-RANS approach to Rayleigh–Bénard convection with wavy bottom walls and a superimposed magnetic field yielded the expected effects on the reorganisation of the eddy structure and consequent modifications of the mean and turbulence parameters and wall heat transfer.

Key words: deterministic eddy structure, numerical simulations, Rayleigh–Bénard and magnetic convection, transient RANS, turbulence control.

1. Introduction

Large-scale eddies can be discerned in many turbulent flows in laboratories, in nature, or in industrial applications. Often, as in the case of vortex shedding, in flows driven by buoyancy or subjected to a magnetic field or system rotation, the large structure has a deterministic character. Such vortical structures also appear in laminar flows, but in turbulent regimes it is not always clear whether these structures can be regarded as true turbulence (smooth spectrum and probability density functions), or they may be interpreted as a form of mean motion with inherent but deterministic (organised, coherent) unsteadiness.

Whatever their nature, these large structures are usually the major carrier of momentum, heat, and species, especially in regions away from a solid wall. Hence, in such flows the transport processes can be controlled by affecting only or primarily the coherent structure. Control can be achieved either by imposing an external force (*distrubuted* control), or by controlling the *boundary* topology or its physical

conditions. Both techniques have long been in use: rotation, buoyancy, electric or magnetic field, surface blowing or suction, riblets and grooves, are only some of the means applied to control drag, heat and mass transfer, entrainment and mixing, combustion, noise, etc. However, it is only recently, with the advancement of experimental field techniques (e.g. Particle Imaging or Tracking Velocimetry, PIV, PTV) and of Direct Numerical and Large Eddy Simulations (DNS, LES), that the flow and turbulence control studies have focussed more on coherent structures. Major prerequisites for the analysis of the effects of coherent structures are the ability to identify the morphology of the organised deterministic motion and a proper interpretation of their role in controlling the flow and transport processes. Once this is achieved, the effects of various methods of flow control can be tested and optimised for the desired performance. While direct numerical simulation and large eddy simulation can provide necessary information, their application in complex industrial flows at higher Reynolds and Rayleigh numbers is still not feasible. On the other hand, the conventional Reynolds-Averaged Navier–Stokes (RANS) approach, which is still used as the major industrial predictive tool, by its virtue, conceals any spectral and structural information, and is regarded as unsuitable for detecting any identifiable eddy structure. A hybrid approach that fully resolves large-scale coherent structures and uses a RANS model to provide the second moments for the remaining – still substantial – part of the spectrum, seems a plausible solution method.

We argue that for flows with identifiable and dominant large eddy structure (vortex shedding, internal separation and recirculation, longitudinal vortices, Rayleigh–Bénard and other types of natural convection, as well as flows with rotation), the application of the Time-dependent Reynolds-Averaged Navier–Stokes (T-RANS) approach can be a useful tool for identifying the organised motion and its response to the imposed distrubuted or boundary control. The approach is akin to Very Large Eddy Simulation (VLES) by which the large structure is fully resolved, whereas the 'rest' of the turbulence is modelled by conventional turbulence closure models ('subscale model'). As compared to LES, here both contributions to the long-term statistical averages are of the same order of magnitude. Close to a solid wall, the large structure is suppressed by wall blockage, and the turbulence production either by mean strain or buoyancy due to wall heating, is dominant. Here, the unresolved incoherent motion bears most of the second moments and they need to be provided by a subscale model. This imposes a special requirement to model accurately the wall phenomena. On the other hand, away from a solid wall, where the freely evolving large structure becomes dominant, this structure should be fully resolved by a time-dependent solution of the 'filtered' equations. Resolving the large-scale motion enables us to capture accurately the large-scale transport, which in conventional RANS methods is usually modelled inadequately by gradient hypotheses.

The approach proposed here is similar to the 'semi-deterministic' turbulence modelling proposed by Ha Minh [1] (see also [2, 3]). Both methods have their roots

in the decomposition of the instantaneous variables into time-mean, unsteady coherent motion, and the remaining random, incoherent fluctuations, as proposed by Hussain [4]. Ha Minh and his coworkers reported the application of their approach to flow behind a backward facing step, where the time-mean and coherent fluctuations were lumped into the ensemble-averaged motion for which the ensemble-averaged Navier–Stokes equations were solved in time. The contribution to the second moment by the unresolved incoherent motion was provided by a modified version of the conventional low-Reynolds number k–ε model, in which the eddy viscosity was reduced by arbitrarily decreasing the empirical coefficient C_μ to a value which enabled unsteady quasi-periodic solutions to be obtained. This has been recognised as a major shortcoming of the Ha Minh approach, since no general modification valid for a broader class of flows could be deduced. The backward-facing step flow may not be the best example for this approach: according to Auburn et al. [3], the experimental conditional sampling indicated that the coherent structure originating from the separated mixing layer, despite deterministic features, 'present significant random discrepancies'. Indeed, for flows with relatively smooth spectrum distribution, and where the coherent structure is not clearly separated in spectral space from the incoherent turbulence, a general modification of the 'subscale' model still needs to be worked out, possibly in terms of scales and energy contents of the resolved coherent and unresolved incoherent motion.

In this work we consider flows where the deterministic coherent structure seems well separated from the incoherent turbulence in spectral space, both in the energy content and in scales. This does not necessarily mean a dip in the spectrum, since the deterministic motion can have a wider range of frequencies which may overlap with the stochastic turbulence. Here, as the results below show, the problem of modifying the single-point turbulence model used for incoherent motion is absent. The flows considered are several cases of steady Rayleigh–Bénard convection which, in addition to the classic case, include configurations with non-flat bottom-wall topology, and with superimposed magnetic field. In all cases the large-scale coherent structure is known to exist and, for some of the cases, the detailed DNS and experimental data are available. Despite similarity in approach, our motivation to explore Rayleigh-Bénard convection with T-RANS was not inspired by the work of Ha Minh and his group (in fact we were unaware of this work when we started). It originated from problems encountered when solving Rayleigh–Bénard convection with conventional steady two-dimensional RANS computations [5], which all yielded a steady roll/cell pattern irrespective of the Rayleigh number, contrary to the experimental observation.

Comparison of T-RANS and DNS statistics, which serves as a first check if the T-RANS approach is meaningful, requires care in interpreting the statistics in order to account for the contribution of the resolved motion. The triple decomposition, by which the instantaneous field is assumed to consist of long-term average (time-mean), quasi-periodic (coherent structure) and random (stochastic) fluctuations, provides a satisfactory tool, indicating that the long-term statistics can be well

reproduced by accounting for both the random and coherent contributions. A second test of applicability of T-RANS is the comparison of structure-identification functions evaluated in parallel with DNS and T-RANS realisations. Various identification criteria have been applied including numerical visualisation, critical point theory and vortex dynamics approaches.

The T-RANS approach yielded a very similar large-scale structure for the classical Rayleigh–Bénard convection as obtained by DNS. The distribution of mean and second-moment quantities and heat transfer on the walls are also in excellent agreement with available DNS and experimental data. Based on this verification, the T-RANS method was then used to predict the effect of the magnetic field and wall waviness on the eddy structure and wall heat transfer in the same flow configuration. Only partial validation of these cases was possible because of a lack of experimental or other data.

2. Equations and Triple Decomposition

The instantaneous motion of an incompressible, conductive fluid under joint action of buoyancy and magnetic force is described by the equations for continuity, momentum, energy, and electric potential:

$$\frac{\partial \hat{U}_i}{\partial x_i} = 0, \tag{1}$$

$$\frac{\partial \hat{U}_i}{\partial t} = \frac{\partial}{\partial x_j}\left(\nu \frac{\partial \hat{U}_i}{\partial x_j} - \hat{U}_i \hat{U}_j\right) - \frac{1}{\rho}\frac{\partial (\hat{P} - P_{\text{ref}})}{\partial x_i} + \beta g_i (\hat{T} - T_{\text{ref}}) + \underbrace{\frac{\sigma}{\rho}\left(-\epsilon_{ijk}\hat{B}_k \frac{\partial \hat{\Phi}}{\partial x_j} + \hat{U}_k \hat{B}_i \hat{B}_k - \hat{U}_i \hat{B}_k^2\right)}_{\hat{F}_i^L}, \tag{2}$$

$$\frac{\partial \hat{T}}{\partial t} = \frac{\partial}{\partial x_j}\left(\frac{\nu}{\text{Pr}}\frac{\partial \hat{T}}{\partial x_j} - \hat{T}\hat{U}_j\right), \tag{3}$$

$$\nabla^2 \hat{\Phi} = \nabla \cdot [\hat{\mathbf{U}} \times \hat{\mathbf{B}}], \tag{4}$$

where $\hat{F}_i^L$ is the Lorentz force, $\hat{\Phi}$ is the electric potential, $\hat{B}_i$ is the imposed magnetic field.

For the resolved ('filtered') motion, equations can be written in essentially the same form as for LES:

$$\frac{\partial \langle U_i \rangle}{\partial x_i} = 0, \tag{5}$$

$$\frac{\partial\langle U_i\rangle}{\partial t} + \langle U_j\rangle\frac{\partial\langle U_i\rangle}{\partial x_j}$$
$$= \frac{\partial}{\partial x_j}\left(\nu\frac{\partial\langle U_i\rangle}{\partial x_j} - \tau_{ij}\right) - \frac{1}{\rho}\frac{\partial(\langle P\rangle - P_{\mathrm{ref}})}{\partial x_i} + \beta g_i(\langle T\rangle - T_{\mathrm{ref}})$$
$$+ \frac{\sigma}{\rho}\left(-\epsilon_{ijk}\langle B_k\rangle\frac{\partial\langle\Phi\rangle}{\partial x_j} + \langle U_k\rangle\langle B_i\rangle\langle B_k\rangle - \langle U_i\rangle\langle B_k^2\rangle\right), \tag{6}$$

$$\frac{\partial\langle T\rangle}{\partial t} + \langle U_j\rangle\frac{\partial\langle T\rangle}{\partial x_j} = \frac{\partial}{\partial x_j}\left(\frac{\nu}{Pr}\frac{\partial\langle T\rangle}{\partial x_j} - \tau_{\theta j}\right), \tag{7}$$

$$\nabla^2\langle\Phi\rangle = \nabla\cdot[\langle\mathbf{U}\rangle\times\langle\mathbf{B}\rangle], \tag{8}$$

where the $\langle\,\rangle$ stands for resolved (implicitly filtered) quantities, and τ_{ij} and $\tau_{\theta j}$ represent contributions due to unresolved scales to the momentum and temperature equations, respectively, which were provided by the subscale model.

Assuming that the large-scale structure has a deterministic character and is distinct in the spectral space from the rest of turbulence, we can decompose the instantaneous flow property at a point $\hat{\Psi}(x_i,t)$ into time-mean $\overline{\Psi}(x_i)$, deterministic $\tilde{\Psi}(x_i,t)$, and random (incoherent) $\psi(x_i,t)$, i.e.

$$\hat{\Psi}(x_i,t) = \overline{\Psi}(x_i) + \tilde{\Psi}(x_i,t) + \psi(x_i,t) = \langle\Psi\rangle(x_i,t) + \psi(x_i,t). \tag{9}$$

By performing a long-time averaging at a point in space and assuming that the coherent and random motion are not directly interacting, the second moments are obtained as a sum of the resolved and modelled contributions, as follows from the long-term averaging, i.e. for variables Ψ and Υ:

$$\overline{\hat{\Psi}\hat{\Upsilon}} = \overline{\overline{\Psi}\,\overline{\Upsilon}} + \overline{\tilde{\Psi}\tilde{\Upsilon}} + \overline{\psi\gamma} = \overline{\langle\Psi\rangle\langle\Upsilon\rangle} + \overline{\psi\gamma}. \tag{10}$$

Unlike in LES, both contributions, i.e. the coherent (resolved) and the random (modelled), are usually of the same order of magnitude and, close to a wall, the unresolved part is larger, as is shown later in the case of turbulent heat flux and temperature variance.

In order to illustrate the implication of the approach we consider the long-term averaged energy equation, which for steady Rayleigh–Bénard convection reduces to

$$\frac{\partial}{\partial x_j}\left(\frac{\nu}{\mathrm{Pr}}\frac{\partial\overline{\langle T\rangle}}{\partial x_j} - \overline{\overline{T}\,\overline{U}_j} - \overline{\tilde{T}\tilde{U}_j} - \overline{\tau}_{\theta j}\right) = 0, \tag{11}$$

where $\overline{\tau}_{\theta j} = \overline{\theta u_j}$. The first three terms are provided from a time-dependent, three-dimensional numerical solution of resolved quantities and the last term is provided

by the single-point 'subscale' model. Further averaging over homogeneous (horizontal) planes yields the expression for the total heat flux in vertical direction (z) (with $\overline{\tau}_{\theta w} = \overline{\theta w}$):

$$\frac{\nu}{\mathrm{Pr}}\frac{\partial \overline{\langle T \rangle}}{\partial z} - \overline{\tilde{T}\tilde{W}} - \overline{\tau}_{\theta w} = \frac{q_w}{\rho c_p} = \text{const.} \tag{12}$$

Hence, the long-term total vertical heat flux, averaged over horizontal planes (constant in a steady Rayleigh–Bénard convection), consists of molecular, large-scale (coherent) and small-scale (modelled) contributions.

3. The 'Subscale' Model and Solution Method

Because only the largest scales are fully resolved in time and space, care must be taken to provide an adequate 'subscale' model for the remaining, relatively large, unresolved part of the turbulence spectrum. In the near-wall region, the direct effect of the large-scale structure is small and the subscale model provides an almost complete contribution to the turbulent transport of momentum, heat and species. Hence, the importance of the subscale model is much greater than, for example, the subgrid scale model in LES. Besides, the subscale model should not be dependent on the grid size, as it is in LES, simply because the unresolved motions span over a larger range of scales than defined by the numerical mesh. It seems natural to use a single-point closure as practised in the RANS approach. As mentioned in the Introduction, in some flows where the coherent structure is not so dominant and the spectrum has a smooth shape, the single-point closure model may need to be modified to reduce the modelled contribution (e.g., [2]). However, this is not necessary in the present case. Moreover, because the turbulent transport by large-scale motion is fully resolved, and the importance of the subscale model is particularly significant close to the wall where the mean convection is often negligible, there is no need to solve differential transport equations for second moments (turbulent stress, heat flux) and a simple algebraic model seems to be adequate. The study reported here was performed using a 'reduced' algebraic expression for heat flux $\tau_{\theta j}$ derived by truncation of the modelled differential transport equation for $\tau_{\theta j}$ by assuming weak equilibrium, but retaining all major flux production terms (all treated as time-dependent):

$$\tau_{\theta i} = -C_\phi \frac{\langle k \rangle}{\langle \varepsilon \rangle}\left[\tau_{ij}\frac{\partial \langle T \rangle}{\partial x_j} + \xi\,\tau_{\theta j}\frac{\partial \langle U_i \rangle}{\partial x_j} + \eta(\beta g_i \langle \theta^2 \rangle + \langle \theta f_i^L \rangle)\right], \tag{13}$$

where

$$f_i^L = \mathbf{j} \times \mathbf{B} = \frac{\sigma}{\rho}(\underbrace{-\nabla\phi_e}_{\mathbf{e}} + \mathbf{u} \times \mathbf{B}) \times \mathbf{B} \tag{14}$$

is the fluctuating Lorentz force, and $\mathbf{e}$ is the fluctuating electric field. Note that $\mathbf{B}$ stands for $\hat{\mathbf{B}} = \overline{\mathbf{B}}$, assumed to be independent of (or slowly varying with) time.

The turbulent stress tensor τ_{ij} and the correlations involving the electric field $\langle u_i e_j \rangle$ and $\langle \theta e_j \rangle$ should also be expressed in similar algebraic forms by truncation of the full transport equations for these quantities (here $\langle\ \rangle$ means that the modelled expressions use resolved quantities). However, in the present work we use the simple eddy diffusivity expressions for these moments and account for the buoyancy and magnetic field by additional terms in the transport equations for the turbulence kinetic energy $\langle k \rangle$ and its dissipation rate $\langle \varepsilon \rangle$ [6]. These two equations, together with the equations for temperature variance, $\langle \theta^2 \rangle$, (all modified for low-Re number and near-wall effects), close the problem, resulting in a three-equation model, $\langle k \rangle - \langle \varepsilon \rangle - \langle \theta^2 \rangle$:

$$\frac{D\langle k \rangle}{Dt} = \mathcal{D}_k + P_k + G_k^g + G_k^L - \langle \varepsilon \rangle, \tag{15}$$

$$\frac{D\langle \theta^2 \rangle}{Dt} = \mathcal{D}_\theta + P_\theta - \langle \varepsilon_\theta \rangle, \tag{16}$$

$$\frac{D\langle \varepsilon \rangle}{Dt} = \mathcal{D}_\varepsilon + P_{\varepsilon 1} + P_{\varepsilon 2} + G_\varepsilon^g + G_\varepsilon^L - Y, \tag{17}$$

where $\mathcal{D}$ stands for diffusion, P is production by mean field gradients, G is production by body force (G^g-buoyancy, G^L-Lorentz force), $\langle \varepsilon \rangle$ is turbulence energy dissipation, and Y is the destruction of $\langle \varepsilon \rangle$. All these terms are defined by conventional expressions (see, e.g., [7]) using standard coefficients and the thermal-to-mechanical turbulence time-scale ratio $R = \langle \theta^2 \rangle \langle \varepsilon \rangle / 2 \langle k \rangle \langle \varepsilon_\theta \rangle = 0.5$. A novelty is the model of production by the Lorentz force both in the $\langle k \rangle$ and $\langle \varepsilon \rangle$ equations [6]:

$$G_k^L = -\frac{\sigma}{\rho} B_0^2 \langle k \rangle \exp\left(-C_L \frac{\sigma}{\rho} B_0^2 \frac{\langle k \rangle}{\langle \varepsilon \rangle} \right), \tag{18}$$

$$G_\varepsilon^L = -\frac{\sigma}{\rho} B_0^2 \langle \varepsilon \rangle \exp\left(-C_L \frac{\sigma}{\rho} B_0^2 \frac{\langle k \rangle}{\langle \varepsilon \rangle} \right), \tag{19}$$

with $C_L = 0.025$.

The equation set is solved numerically using a finite-volume Navier–Stokes-Maxwell solver for three-dimensional flows in structured non-orthogonal geometries, with Cartesian vector and tensor components and a collocated variable arrangement. The second-order accurate central difference scheme (CDS) was applied for the discretisation of diffusive terms in all equations and of convective terms in $\langle U, V, W, T, \Phi \rangle$ equations. The second-order linear-upwind scheme (LUDS) was applied for convective terms in equations for the turbulence quantities, i.e. $\langle k, \varepsilon, \theta^2 \rangle$.

The time marching is performed by fully implicit second-order three-time-level method which allows larger time steps to be used, in view of the fact that only large scales are being resolved. The typical non-dimensional time step was $\tau^* = 0.02$, where $\tau^* = \tau \sqrt{\beta g \Delta T / H}$. Test with much smaller and larger time steps (0.005 and 0.08) showed no noticeable difference in long-term averaged

properties, nor in structure morphology. Typical computations covered about 200–400 non-dimensional time units τ^* which correspond roughly to 15–30 convective time scales based on convective velocity and characteristic cell circumference, defined by Kerr [8]. In all cases, the temperature of the walls were kept constant at a predefined level to yield the desired Rayleigh numbers. All computations started with uniform fluid temperature.

4. Illustrations

4.1. The classic Rayleigh–Bénard convection

The T-RANS computations of Rayleigh–Bénard convection over a heated flat bottom wall at a range of Rayleigh numbers reproduced very well the mean temperature, wall heat transfer, and the second moments obtained by experiments and DNS. This is illustrated in Figure 1 where the mean temperature, computed with T-RANS for two Ra numbers, 10^7 and 10^9, ($\mathrm{Ra} = \beta g_i \Delta T \,\mathrm{Pr}\, H^3/\nu^2$), are compared in linear and semi-logarithmic plot with the DNS data of Grötzbach [9] for $\mathrm{Ra} = 3.8 \times 10^5$ and Wörner [10] for $\mathrm{Ra} = 6.5 \times 10^5$. Despite a large difference in Rayleigh numbers, the T-RANS computations are in excellent agreement with the DNS data when normalised with the buoyancy temperature $T_q = Q/U_q$ and length scale $Z_q = \alpha/U_q$, where Q is the wall heat flux, and $U_q = (\beta\alpha^2 g Q/\nu)^{1/4}$ is the buoyancy velocity. A similar quality of agreement was obtained for the turbulent thermal heat flux and temperature variance (Figure 2). Both parts of the figure illustrate the contributions of the resolved and modelled motion to the second moments. It is noted that the modelled contribution dominates the near-wall region accounting almost fully for the total turbulent heat flux and temperature variance, whereas the resolved contribution becomes dominant away from the wall. Note that the heat flux is shown on a blown-up scale only for the near-wall region; the profile for the complete channel section is shown in Figure 6.

Moreover, the parallel application of several structure identification methods (second invariant of the velocity gradient, discriminant of its characteristic equation, kinematic vorticity number, massless particle trajectories) to the instantaneous fields obtained by DNS and T-RANS, showed a striking resemblance in the large structure, including the spiralling updrafts as major constituents of the large-scale unsteady roll-cell pattern [11, 12]. An illustration is provided in Figures 3–5 where examples of the instantaneous plots of trajectories of massless particles are shown for several horizontal and vertical planes obtained by DNS and T-RANS for the same Ra number. The figures show a number of organised vortical structures with clearly identifiable vortex cores both in horizontal and vertical planes. These quantitative and qualitative agreements between T-RANS and DNS (more details can be found in [12, 13]) ensured confidence in the T-RANS approach and its extrapolation to cases with multiple-body forces and complex wall topology, which are both expected to impose a reorganisation and a modification of the large coherent structure. Because this structure provides major ‘communication’ between the boundary

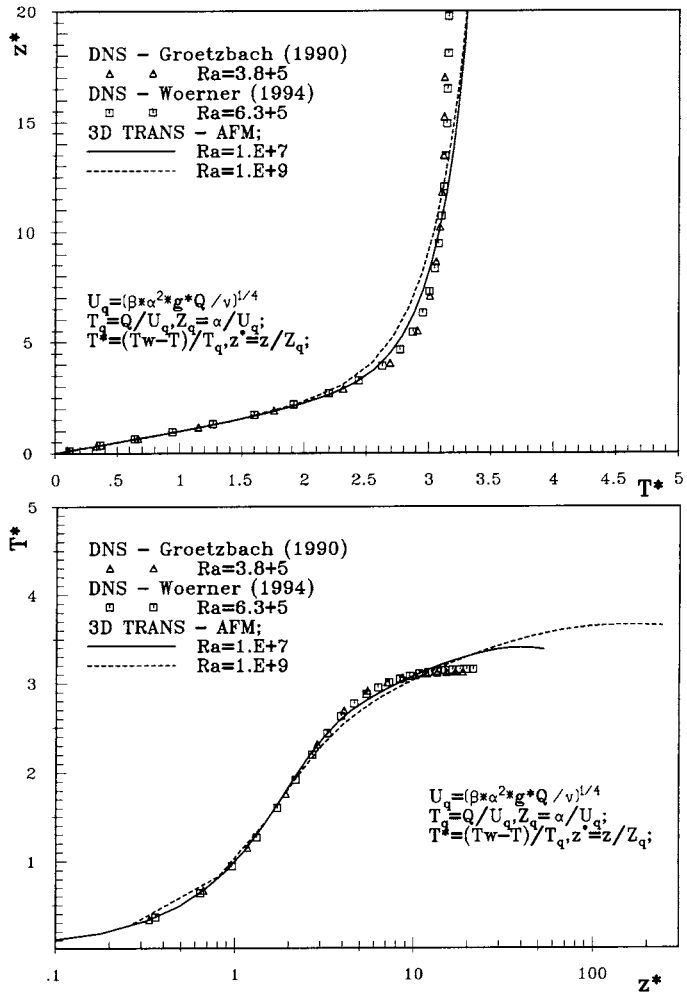

Figure 1. Mean temperature profiles in RB convection; T-RANS and DNS – Grötzbach [9], Wörner [10].

layers at the bottom and top walls, its modification is expected to influence the overall heat transfer.

4.2. Rayleigh–Bénard convection subjected to Lorentz force

The next case considered is an example of *distributed* turbulence control: a magnetic field imposed on the flow of conductive fluid generates the Lorentz force, which dampens the velocity and its fluctuations in the direction of the force [14]. As a consequence, the vortical structure is modified with a tendency to align the major vortex axis with the direction of the magnetic field vector. This effect is currently utilised in controlling the process of continuous metal casting and is

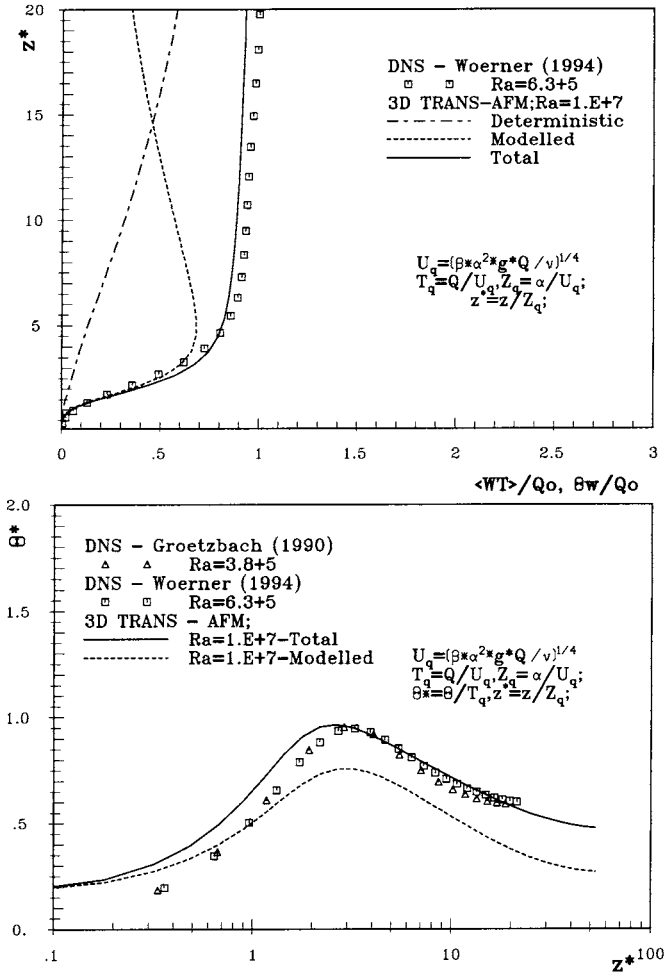

Figure 2. Long-term averaged profiles of vertical heat flux (near-wall blow-up) and the temperature variance in RB convection; T-RANS and DNS – Grötzbach [9], Wörner [10].

regarded as a potential means to control the crystal growth in a large crucible. The algebraic turbulence model used here was developed to reproduce the effect of magnetic field on mean velocity and turbulent stresses in forced turbulent flow in a plane and a square channel [6]. In addition to the direct effect on large-scale motion (Lorentz force in momentum equations), it is noted that the additional 'magnetic' terms representing the effects of the magnetic field are also present in the model equations for turbulent kinetic energy and its dissipation rate, as well as in the model expressions for other second moments.

Here we present a case of magnetic Rayleigh–Bénard convection (RBM), i.e. the situation where the gravitational vector and the imposed magnetic field are aligned. The considered Ra number, 10^7, ensures a fully turbulent regime in the ab-

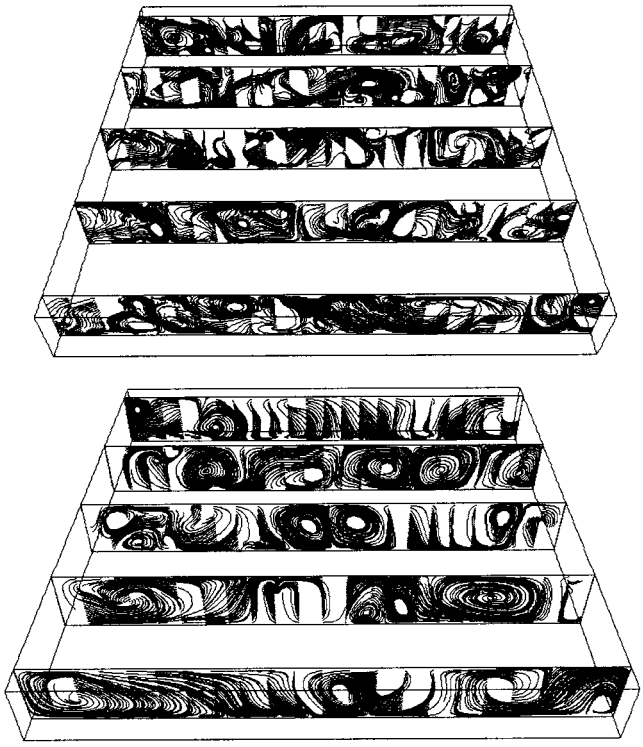

Figure 3. Instantaneous trajectories of massless particles in five vertical planes for DNS [10] (top) and T-RANS realisations (bottom), Ra $= 6.5 \times 10^5$, Pr $= 0.71$.

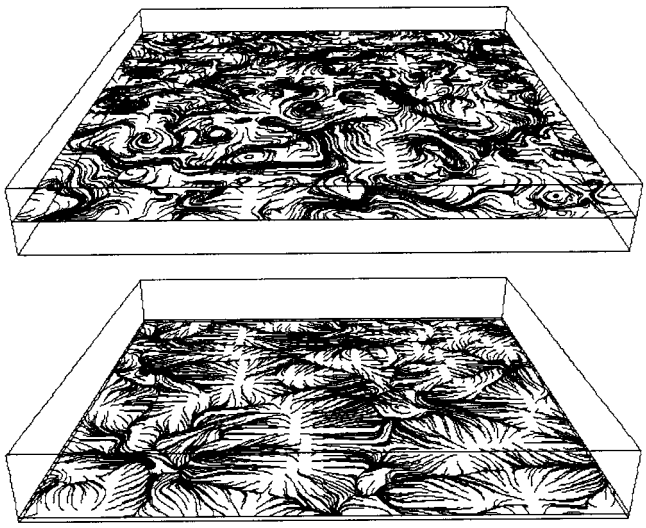

Figure 4. Instantaneous trajectories of massless particles in two horizontal planes for DNS [10] realisation, Ra $= 6.5 \times 10^5$, Pr $= 0.71$, $z/H = 0.5$ (top) and 0.05 (bottom).

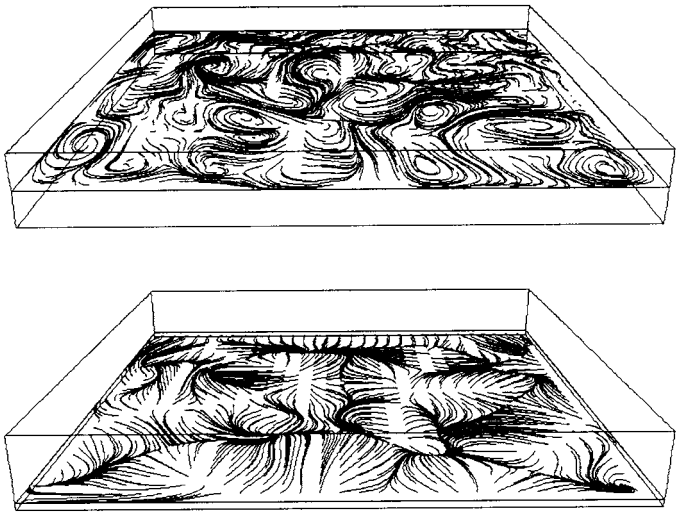

Figure 5. Instantaneous trajectories of massless particles in two horizontal planes for T-RANS realisation, Ra $= 6.5 \times 10^5$, Pr $= 0.71$, $z/H = 0.5$ (top) and 0.05 (bottom).

sence of magnetic field, thus enabling the study of the effect of the Lorentz force on the reorientation of the vortical structure and the associated transport phenomena. We consider three cases corresponding to zero, medium and strong magnetic fields, defined by Hartmann number Ha $= 0$, 20 and 100 (Ha $= B_0 H\sqrt{\sigma/\rho\nu}$). Figure 6 shows the turbulent heat flux and temperature variance across the channel for three Ha numbers, all normalised with the wall heat flux (that equals the total long-term averaged heat flux across the flow) for the case of no magnetic field (Ha $= 0$). The resolved and modelled contributions, as well as their sum (the complete turbulence second moments) are plotted separately. Note that Figure 6a shows the same results as Figure 2, but now plotted over the whole channel. Because the vertical distance is here scaled with the channel width D, the T-RANS computations for Ra $= 10^7$ do not collapse to DNS data (symbols) that were performed for Ra $= 6.5\times10^5$. The difference between the complete turbulent heat flux and the total flux (equal to 1) represents the molecular flux. The effect of the magnetic field is clearly manifested in the reduction of the total heat flux, as a consequence of the reduction in both the resolved and modelled contributions. The modelled parts are the main contribution in the near-wall regions ($0 < z/D \leq 0.1$, $0.9 \leq z/D < 1$) for the situation without a magnetic field, (Ha $= 0$). When the magnetic field is active, the 'magnetic terms' in the model of the unresolved motion dampen the modelled contribution relative to the resolved one. For Ha $= 20$, both contributions are equally important in the near-wall regions for both

$$\overline{\theta w}_{\rm tot} = \overline{\tau}_{\theta w} + \overline{\tilde{T}\tilde{W}} \quad \text{and} \quad \overline{\theta^2}_{\rm tot} = \overline{\langle\theta^2\rangle} + \overline{\tilde{T}\tilde{T}},$$

where

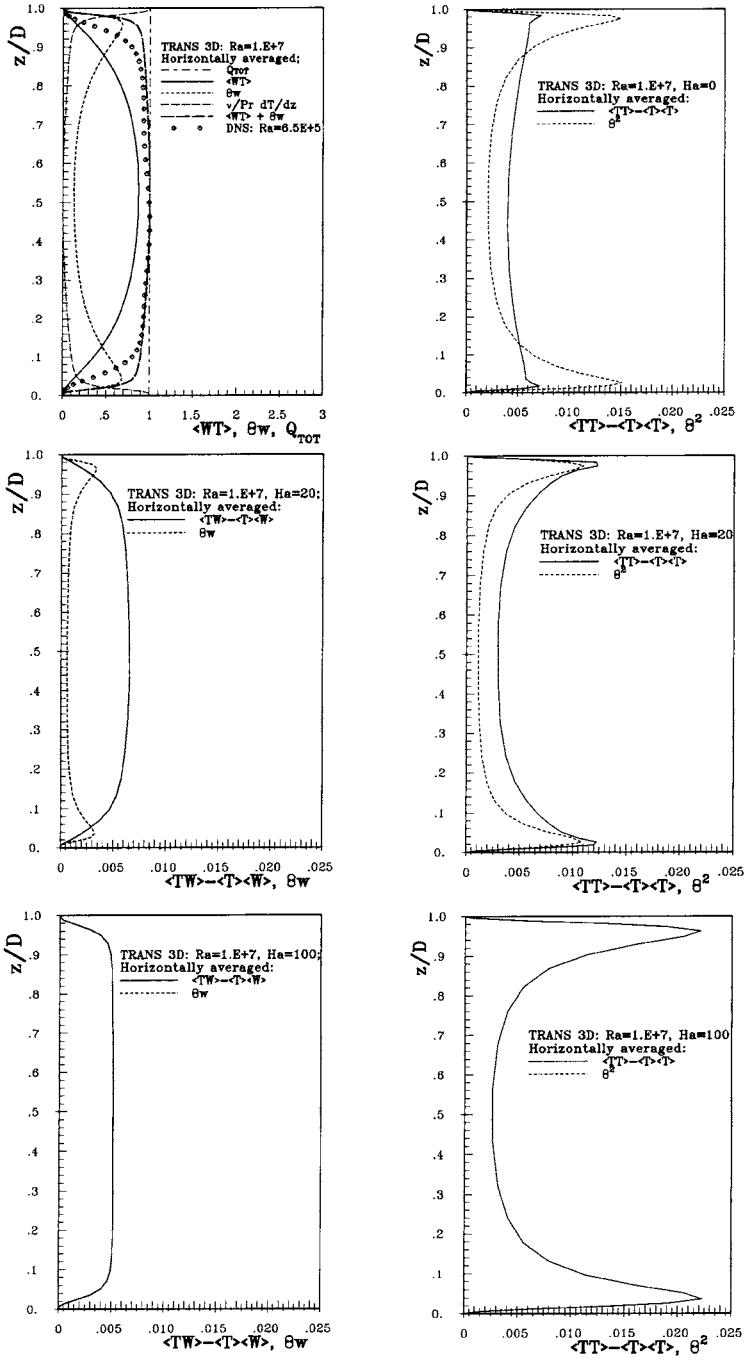

Figure 6. Effect of the transversal magnetic field on long-term averaged deterministic and modelled contributions to vertical heat flux and temperature variance, $\mathrm{Ra} = 10^7$, $\mathrm{Ha} = 0$, 20, 100; modelled contributions (- - -): $\overline{\langle\theta w\rangle}$, $\overline{\langle\theta^2\rangle}$, deterministic contributions (—): $\overline{\tilde{W}\tilde{T}}$, $\overline{\tilde{T}\tilde{T}}$.

$$\overline{\tilde{W}\tilde{T}} = \overline{\langle W\rangle\langle T\rangle} - \overline{\langle W\rangle}\,\overline{\langle T\rangle} \quad \text{and} \quad \overline{\tilde{T}\tilde{T}} = \overline{\langle T\rangle\langle T\rangle} - \overline{\langle T\rangle}\,\overline{\langle T\rangle}$$

represent the deterministic contributions. A further increase in the magnet strength leads to a drastic reduction in the modelled contribution, which becomes negligible at Ha = 100. It is noted that the modelled contribution diminishes faster than the resolved one. This is, of course, the consequence of the model used, which contains damping functions related to the turbulence Reynolds number. A strong damping of the modelled contribution indicates a strong diminishing of the turbulence Re number, reflecting an overall damping of the turbulence kinetic energy associated with unresolved scales. However, the persistence of the contribution by the resolved motion indicates the persistence of the large eddies, which, although subject to reorganisation, still contribute to the second moments. It is interesting to note that the peaks of the temperature variance $\overline{\tilde{T}\tilde{T}}$ for the largest value of Ha are moved away from the walls, which in classic Rayleigh–Bénard convection, is associated with a decrease in Ra number.

The reorganisation is clearly illustrated in Figure 7, showing the planform structures and hot finger-like plumes in between identified by the temperature isosurfaces. Due to the Lorentz force in the x–y plane (since the imposed magnetic field is oriented in the vertical z-direction), the horizontal movement of thermal plumes is significantly reduced. At the same time, the thermal plumes become significantly smaller, but more extended in the vertical direction, with a higher concentration in the near-wall regions. This is reflected in the form and size of the planform structure, which becomes smaller as the strength of the magnetic field increases. The plumes show a tendency towards the cylindrical shape elongated in the vertical direction with aligned vertical velocity and vorticity with the magnetic field and gravitational buoyancy vectors. The coherent structures, identified by the contours of constant kinematic vorticity number, show a very similar behaviour (not shown here). This reorganisation of the plume structure with an increase in the magnetic field has been observed earlier. For example, Chandrasekhar reported (albeit for much lower Ra numbers), that "the cells tend to become narrow and elongated as Ha increases" [15, p. 177].

The effect on the long-term averaged mean temperature is depicted in Figure 8 (top), showing a tendency toward inversion. The application of an eddy-diffusivity concept would result here in a counter-gradient vertical heat flux, which is wrong, illustrating clearly the inadequacy of the eddy diffusivity approach to model the Rayleigh–Bénard and similar phenomena. The effect on wall-heat transfer is illustrated in Figure 8 (bottom) where the time evolution of the Nusselt number is presented. It is obvious that the magnetic field significantly dampens heat transfer, though the effect does not scale linearly with the strength of the imposed magnetic field. It should be noted that the computations started with a uniform temperature and zero velocity field and with a step elevation in the bottom-wall temperature, so that the initial period reflects the development phase. However, in the later period, after $\tau^* \approx 150$, the Nusselt numbers reach almost constant values. For

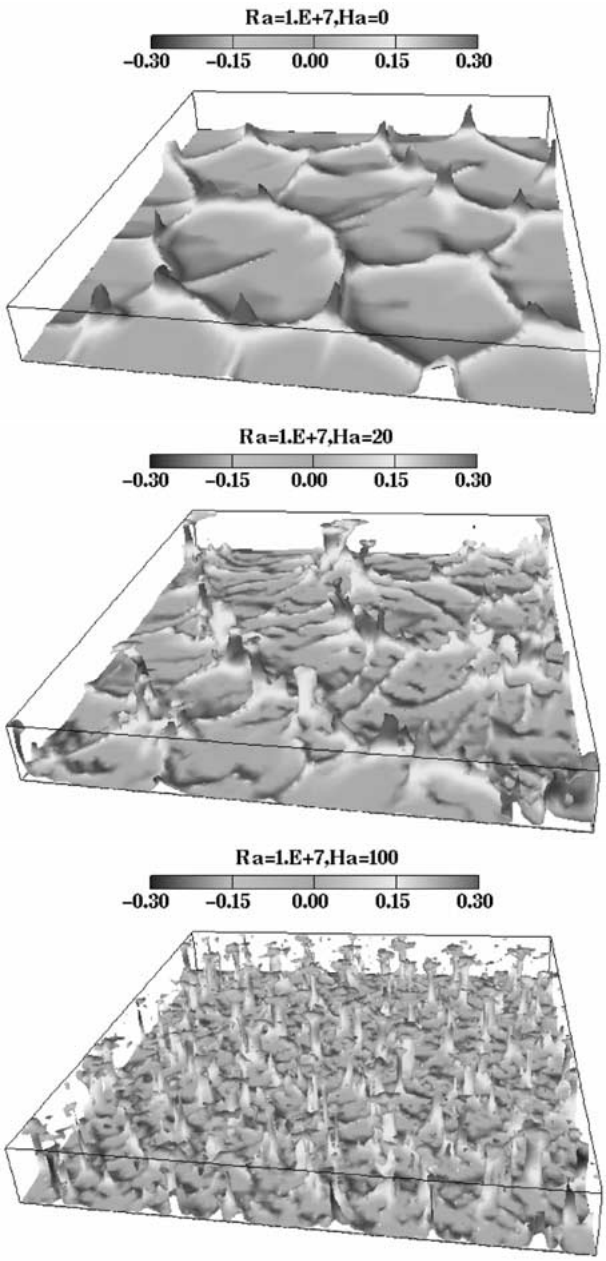

Figure 7. Effect of the transversal magnetic field on planform structures and fingerlike plumes (the isosurface of temperature $T^* = 0.625$ coloured with W), Ra $= 10^7$, $Ha = 0, 20, 100$.

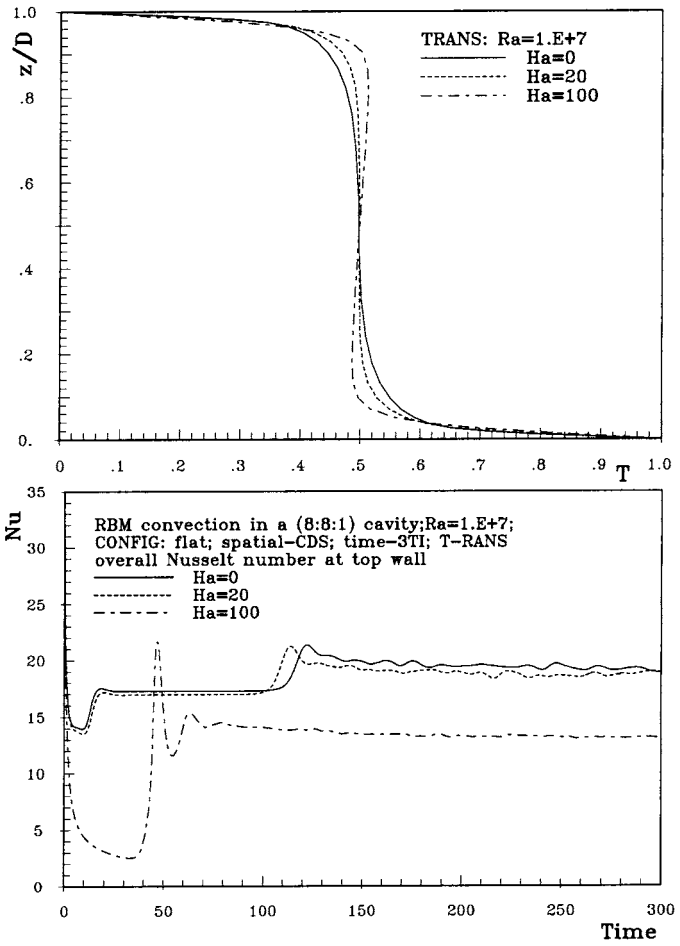

Figure 8. Influence of the transversal magnetic field on long-time averaged temperature profiles (top) and time evolution of integral Nusselt number (bottom).

the classic Rayleigh–Bénard convection the Nu number agrees well with the DNS and experimental correlations. With an increase in Ha number, the Nu number decreases. The effect at Ha $=$ 20 is small, but at Ha $=$ 100 the averaged value of the Nusselt number is close to that for laminar regimes corresponding to much lower Rayleigh numbers. Figure 7, however, shows that the flow contains a distinct eddy structure of a relatively uniform scale, which is nearly two-dimensional. This is also illustrated in Figure 9 which shows examples of the instantaneous distribution of Nusselt numbers on the bottom wall for the three Ha numbers considered. In all three cases, the Nusselt numbers exhibit sharp peaks corresponding to the impingement of plumes on the wall, with very low values in between. However, the space between the peaks and valleys, reflecting the size of the plume patterns, is much smaller at the highest Ha number than in the two other cases. The bottom il-

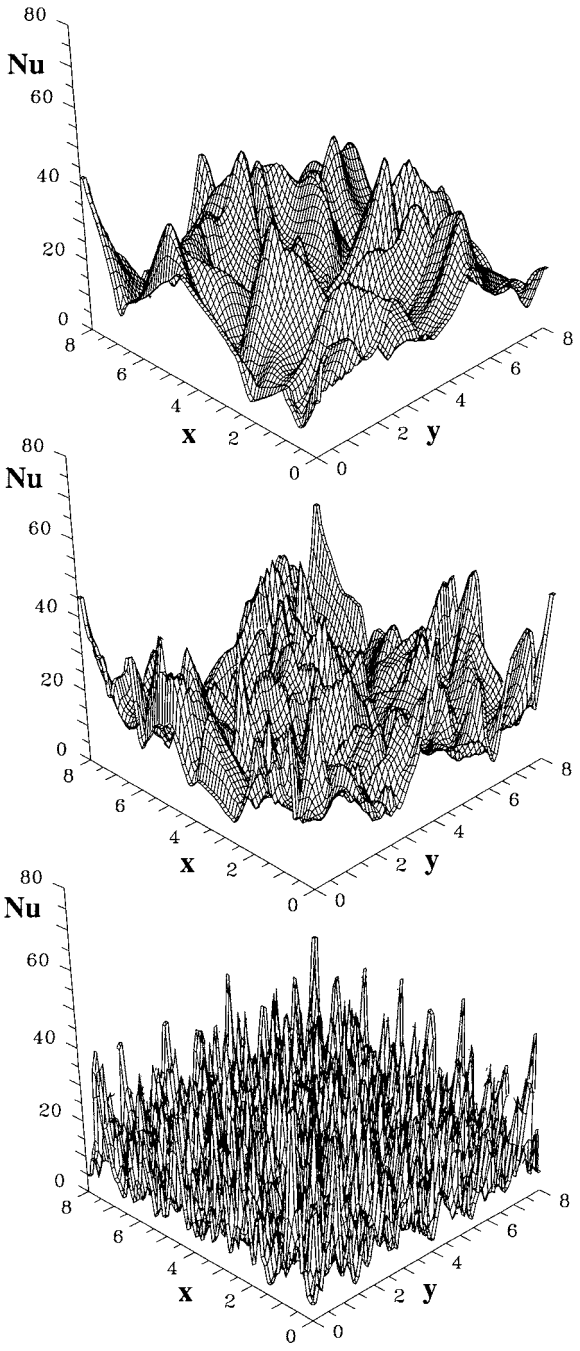

Figure 9. Influence of the transversal magnetic field on the local Nusselt number distribution ($\mathrm{Ra} = 10^7$, $\mathrm{Ha} = 0, 20, 100$).

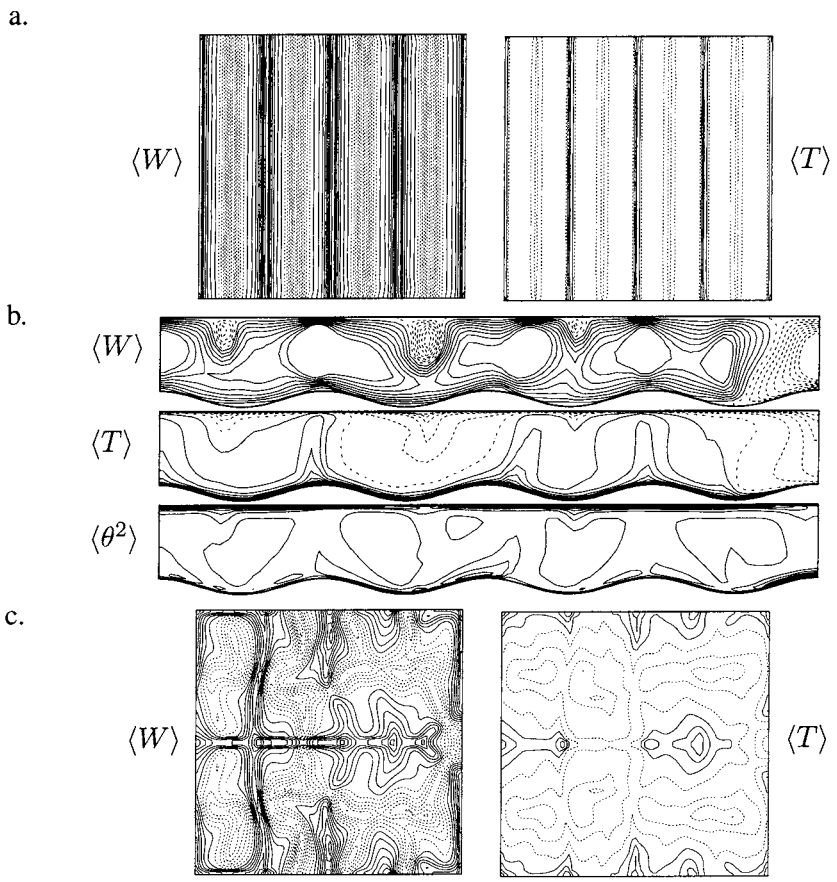

Figure 10. Effect of bottom-wall configuration on first- $\langle W \rangle$, $\langle T \rangle$ and second-order statistics $\langle \theta^2 \rangle$, two-dimensional waviness, $S_B = 0.1\cos(x\pi)$, Ra $= 10^7$, Pr $= 0.71$, (a) $\tau^* = 50$, (b) and (c) $\tau^* = 200$.

lustration in Figure 9 also shows a high degree of order, with peaks of similar values and evenly distributed over the wall surface, corresponding to the well-organised nearly-two-dimensional vertical plumes.

4.3. CAPTURING THE EFFECTS OF WALL TOPOLOGY

As an example of *boundary controlled structure*, we consider a high Ra number (up to Ra $= 10^9$) Rayleigh–Bénard convection over heated wavy walls with different wavelengths and amplitudes. The two- and three-dimensional topologies are defined by sinusoidal surface variation in one and two directions, $S_B = 0.1\cos(x\pi)$, and $S_B(x, y) = 0.1\cos(x\pi)\cos(y\pi)$, respectively. Krettenauer and Schumann [17] performed DNS and LES of the same two-dimensional configuration, though at a much lower Ra number, Ra $= 5.5 \times 10^4$, and observed that the gross feature of

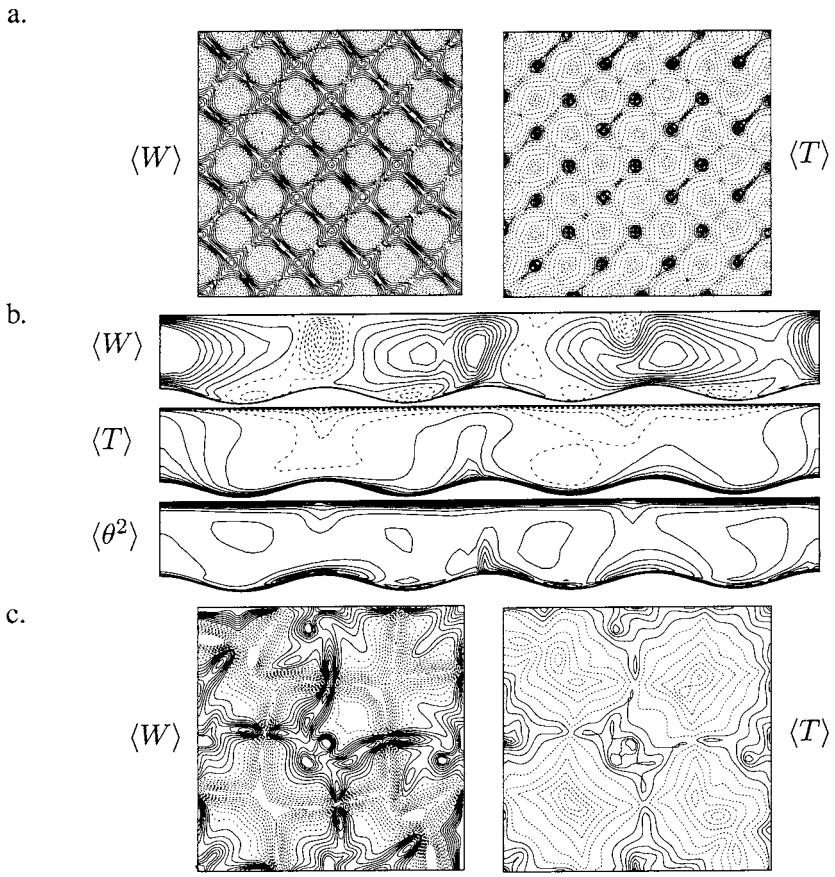

Figure 11. Effect of bottom-wall configuration on first $\langle W \rangle$, $\langle T \rangle$ and second-order statistics $\langle \theta^2 \rangle$, three-dimensional waviness, $S_B = 0.1 \cos(x\pi) \cos(y\pi)$, Ra $= 10^7$, Pr $= 0.71$, (a) $\tau^* = 50$, (b) and (c) $\tau^* = 200$.

the flow statistics, such as the profiles of turbulence variance and fluxes were not very sensitive to the variations of the bottom-wall topology. On the other hand, the motion structure persisted considerably longer over the wavy terrain than over flat surfaces.

The effect of the bottom-wall configuration on the resolved properties $\langle W \rangle$, $\langle T \rangle$ and second moments $\langle \theta^2 \rangle$ is presented in Figures 10 and 11. In the initial stage of heating, $\tau^* = 50$, the contours of the vertical velocity and temperature in the horizontal plane $(x, y, 0.5)$ show a regular flow pattern determined by the wall configuration (Figures 10a and 11a). Updrafts are represented by solid lines and downdrafts by dashed line contours. The sites of the plume generation are located at the surface wave peaks, as observed by five plumes regularly extending in the vertical direction. At $\tau^* = 200$, the picture is significantly different. The locations of the plume realisation are not fixed anymore, the two-dimensional structure ori-

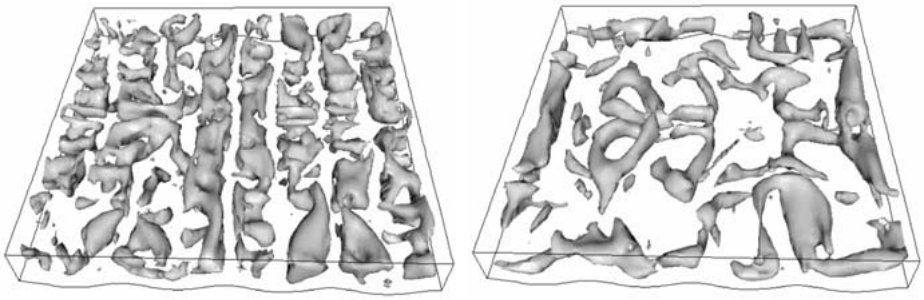

Figure 12. Time evolution and spatial organisation of large coherent structures defined and identified by $\mathcal{N}_k = 2$ at $\tau^* = 50$ (left) and $\tau^* = 200$ (right), two-dimensional waviness, $S_B = 0.1\cos(x\pi)$.

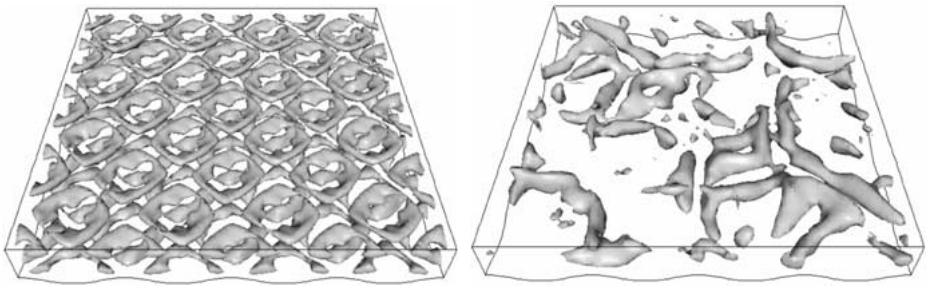

Figure 13. Time evolution and spatial organisation of large coherent structures defined and identified by $\mathcal{N}_k = 2$ at $\tau^* = 50$ (left) and $\tau^* = 200$ (right), three-dimensional waviness, $S_B = 0.1\cos(x\pi)\cos(y\pi)$.

entation is lost, and the plumes' movement produces a strong horizontal motion. The second moments (the modelled part) show a similar behaviour: the contours of $\langle\theta^2\rangle$ in the vertical planes indicate that $\langle\theta^2\rangle$ are concentrated in the near-wall regions. This is what we expected, since the main role of the subscale model is to produce the correct near-wall behaviour, while in the outer region, the large-scale dominated motion is fully resolved. A similar analysis is performed for the three-dimensional surface wave configuration. The plumes rise from the surface peaks and sink into the surface valleys, portraying 25 characteristic locations in the $(x, y, 0.5)$ plane (Figure 11). At $\tau^* = 200$, the initial organisation of the flow cannot be observed anymore. Thermal plumes occupy a significantly larger space and not only the regions close to the bottom surface peaks, as found in the initial phase of flow development.

In order to get a better insight into the organisation and modification of the large coherent structures, we applied the structure identifying analysis to an instantaneous T-RANS realisation. Figures 12 and 13 show the time evolution and spatial organisation of large structures defined and identified by the kinematic vorticity number, $\mathcal{N}_k = \left(|\omega_l|^2/2S_{ij}S_{ij}\right)^{1/2}$. Very different shapes and organisations are observed in the initial stage of heating ($\tau^* = 50$) for two different topologies of the

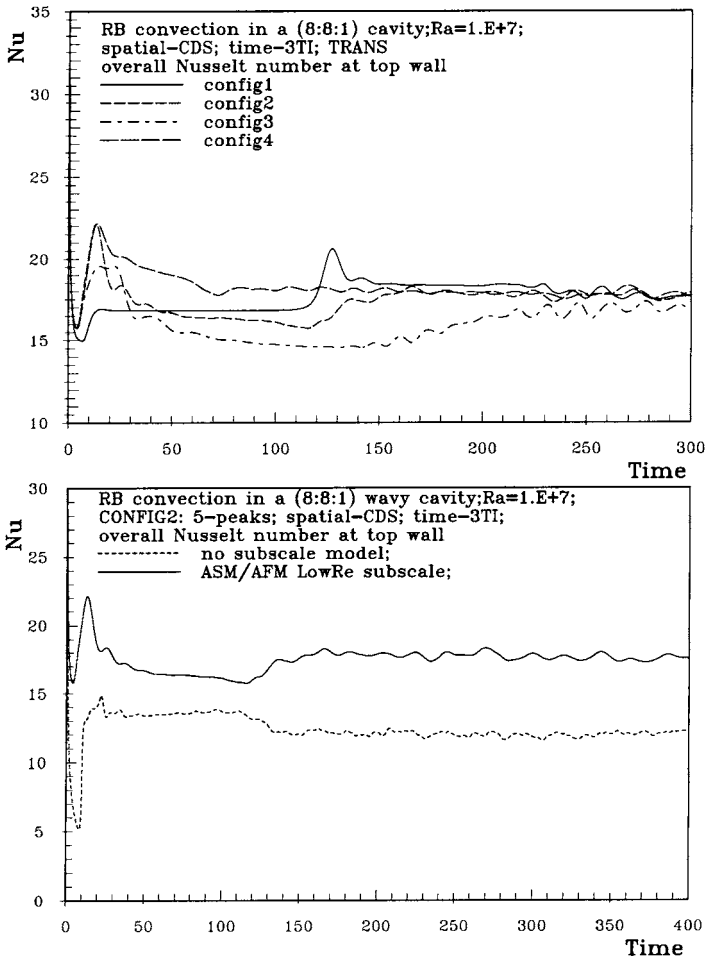

Figure 14. Influence of the bottom-wall topology (top) and of the subscale model on the time evolution of the integral Nusselt number (bottom).

bottom wall. The large two-dimensional structures extending in the y-direction and located in the center of the cavity are observed for the imposed two-dimensional topology. Contrary to this, for three-dimensional wave topology, the coherent structures are located in the near-wall regions and are significantly smaller in size. At $\tau^* = 200$, the structures are very similar in shape and size for both configurations, but even for this time instant, significantly different flow reorganisation can be observed (diagonally oriented for three-dimensional topology and around the central y-axis for two-dimensional wave topology). In both cases and at both time instants, a close correlations between thermal plumes and large structures can be observed.

Figure 14 (top) shows the influence of the bottom-wall topology on the time evolution of integral Nusselt numbers for four different wall configurations: a

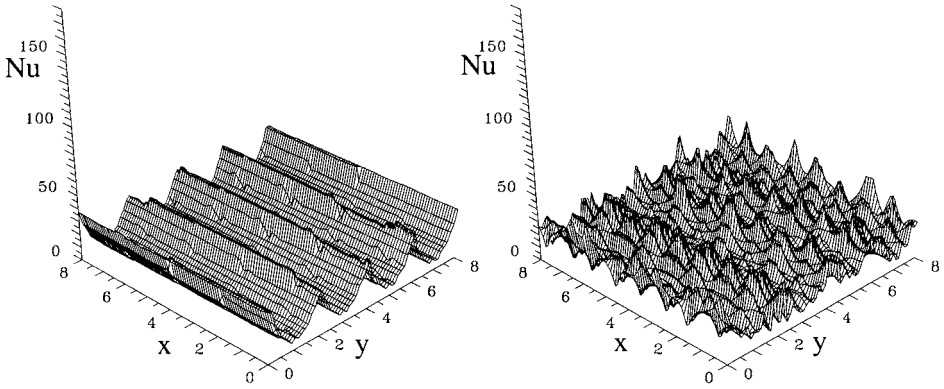

Figure 15. Influence of the bottom-wall topology on local Nusselt number, two-dimensional waviness, $S_B = 0.1\cos(x\pi)$, $\tau^* = 50$ (left) and $\tau^* = 300$ (right).

flat bottom surface (conf1), a two-dimensional wavy surface in the x-direction (conf2), the same configuration with a twice longer wavelength (conf3), and a three-dimensional topology (conf4). The three-dimensional wave configuration promotes a fully developed regime earlier than others. The longer wavelength in two-dimensional surface configuration keeps the initial flow organisation for a very long period of time (almost 200 non-dimensional time units). When the fully developed stage was reached, the integral Nusselt number approached the value for the flat wall, indicating that the imposed waviness of the bottom wall only marginally affects the integral heat transfer at the fully developed stage.

Figure 14 (bottom) illustrates the effect of the 'subscale' model by comparing the 'pseudo DNS' (no subscale model) and T-RANS. Both simulations show an almost identical time response in the development of the overall Nu number, in close correlation with the behaviour of the maximum velocity components. The first peak is observed when the $\langle U \rangle$ and $\langle W \rangle$ velocity components reach their peak values for the first time ($\tau^* = 15$), followed by a decline until the $\langle V \rangle$ velocity reaches its maximum, followed by a subsequent increase in heat transfer. The simulation without a subscale model on a relatively coarse mesh of $82^2 \times 32$ resulted in a laminar-like regime with the averaged overall Nu of 12. In contrast, the simulation with the AFM subscale model produced turbulent flow and more intensive heat transfer yielding a the final averaged value of Nu $= 18$. These findings illustrate the importance of the subscale model in the range of low and transitional Ra numbers for complex geometries, when the grid resolution is not sufficient to resolve all scales. It is also noted that the averaged Nu $= 18$ is close to that for a flat wall at the same Ra number, confirming the findings of Krettenauer and Schumann [17] that the total heat transfer was only marginally affected by the wall waviness (at least for the configurations considered, with relatively small amplitude to wavelength ratio).

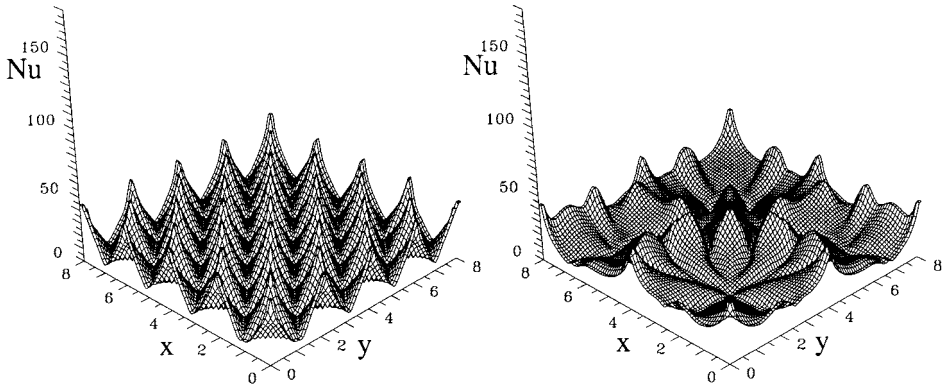

Figure 16. Influence of the bottom-wall topology on local Nusselt number, three-dimensional waviness, $S_B = 0.1\cos(x\pi)\cos(y\pi)$, $\tau^* = 50$ (left) and $\tau^* = 300$ (right).

Finally, Figures 15 and 16 show examples of instantaneous distributions of the Nusselt number for the two- and three-dimensional bottom-wall wave configurations with the same wavelengths, for two time instants. The results are shown for the upper flat cold walls rather than for the bottom wavy walls in order to illustrate the effect of the bottom-wall topology on the heat transfer at the opposite flat wall. Both cases show a strong organisation in the Nusselt number distribution that closely reflects the wall configurations. The organisation in the initial stage ($\tau^* = 50$) is more orderly, but the wall topology effect is also visible much later ($\tau^* = 300$), particularly for two-dimensional waviness. It is also interesting to note that the three-dimensional waviness tends to smooth the Nusselt number distribution at the later stage more efficiently than the two-dimensional topology.

5. Conclusions

The time-dependent Reynolds-averaged Navier–Stokes (T-RANS) approach was applied to analyze the Rayleigh–Bénard convection over a flat and wavy walls, and with superimposed magnetic field, over a range of Rayleigh numbers. The large-scale eddy structure is numerically fully resolved in time and space, whereas the second moments (heat flux, stress, scalar variance) associated with the remaining unresolved turbulence spectrum for velocity and scalar variables are provided by a subscale model for which the single-point three-equation $\langle k\rangle$-$\langle\varepsilon\rangle$-$\langle\theta^2\rangle$ algebraic stress/flux closure was used. Unlike in LES, both the resolved and unresolved contributions are of the same order of magnitude and in the near-wall regions, the contribution of the unresolved part is dominant. This places particular importance on the subscale model, which ought to provide a good reproduction of the near-wall phenomena.

It was demonstrated that the method reproduces very well the long-term averaged mean temperature distribution, wall Nusselt number, turbulence second

moments (heat flux, scalar variance) in classic Rayleigh–Bénard convection that is in excellent agreement with the DNS and experimental data. Moreover, the method captures very well the large-scale coherent structures, with features very similar to those found by DNS. The method was then used to predict the effects of the imposed Lorentz force and bottom-wall waviness on the reorganisation of the large coherent structure, and consequent effects on the mean flow, turbulence statistics and the Nusselt number. The lack of experimental or DNS data for the latter two cases prevents a direct verification of the T-RANS results, but the qualitative effects are in accordance with the observations reported in the literature.

A major advantage of the method is in resolving the dominant large-scale transport, dispensing with a need to use gradient transport hypotheses. On the other hand, because only very large scales are resolved numerically, the approach is more economical than LES: it does not require very fine mesh except close to a solid wall (but only in the wall-normal direction). The time marching can be performed with a larger time step using implicit schemes. In addition, because the resolved large-scale structure is expected to be coherent with a deterministic character, the number of realisations needed to obtain the statistics should be significantly smaller than required for LES. The approach is regarded as potentially useful for many types of flows where the large-scale coherent structure is present: in flows dominated by body forces, in periodic separating and vortex shedding flows, and in large combustion installations prone to instabilities and unsteadiness. Another potential application is in studying and optimising the control of turbulent flow, heat, and mass transfer through the control of large coherent eddy structures.

Acknowledgment

The research of Dr. Saša Kenjereš has been made possible by a fellowship of the Royal Netherlands Academy of Arts and Sciences (KNAW).

References

1. Ha Minh, H., Order and disorder in turbulent flows: their impact on turbulence modelling. In: *Osborn Reynolds Centenary Symposium*, UMIST, Manchester, U.K., May 24th (1994).
2. Ha Minh, H. and Kourta, A., Semi-deterministic turbulence modeling for flows dominated by strong organized structures. In: Durst, F., Kasagi, N., Launder, B.E., Schmidt, F.V., Suzuki, K. and Whitelaw, J.H. (eds), *Proceedings 9th International Symposium on Turbulent Shear Flows*, Kyoto, Japan. Springer-Verlag, Berlin (1993) Vol. 1., pp. 10.5.1–10.5.6.
3. Aubrun, S., Kao, P.L., Ha Minh, H. and Boisson, H., The semi-deterministic approach as way to study coherent structures: Case of a turbulent flow behind a backward-facing step. In: Rodi, W. and Laurence, D. (eds), *Engineering Turbulence Modelling and Experiments 4*. Elsevier, Amsterdam (1999) pp. 491–500.
4. Hussain, A.K.M.F., Coherent structures – Reality and myth. *Phys. Fluids* **26** (1983) 2816–2850.
5. Kenjereš, S. and Hanjalić, K., Convective rolls and heat transfer in finite-length Rayleigh–Bénard convection: A two-dimensional numerical study. *Phys. Rev. E* **62**(6) (2000) 7987–7998.

6. Kenjereš, S. and Hanjalić, K., On the implementation of effects of Lorentz force in turbulence closures models. *Internat. J. Heat Fluid Flow* **21**(3) (2000) 329–337.
7. Hanjalić, K., Achievements and limitations in modelling and computing of buoyant turbulent flows and heat transfer (Special Keynote Lecture). In: Hewitt, G. (ed.), *Proceedings 10th International Heat Transfer Conference*. IChem/Taylor & Francis, London (1994) Vol. 1, pp. 1–18.
8. Kerr, M.R., Rayleigh number scaling in numerical convection. *J. Fluid Mech.* **310** (1996) 139–179.
9. Grötzbach, G., Direct numerical simulation of laminar and turbulent Bénard convection. *J. Fluid Mech.* **119** (1982) pp. 27–53 (Database published in 1997).
10. Wörner, M., Direkte Simulation turbulenter Rayleigh–Bénard Konvektion in flüssigem Natrium. Ph.D. Thesis, University of Karlsruhe, KfK 5228, Kernforschungszentrum Karlsruhe (1994).
11. Cortese, T. and Balachandar, S., Vortical nature of thermal plumes in turbulent convection. *Phys. Fluids A* **5**(12) (1993) 3226–3232.
12. Kenjereš, S. and Hanjalić, K., Identification and visualisation of coherent structures in Rayleigh–Bénard convection with a time dependent RANS. *J. Visualisation* **2**(2) (1999) 169–176.
13. Kenjereš, S. and Hanjalić, K., Transient analysis of Rayleigh–Bénard convection with a RANS model. *Internat. J. Heat Fluid Flow* **20**(3) (1999) 329–340.
14. Mößner, R. and Müller, A numerical investigation of three-dimensional magnetoconvection in rectangular cavities. *Internat. J. Heat Mass Transfer* **42** (1999) 1111–1121.
15. Chandrasekhar, S., *Hydrodynamic and Hydromagnetic Stability*. Dover Publications, New York (1981).
16. Hanjalić, K. and Kenjereš, S., Reorganization of turbulence structure in magnetic Rayleigh–Bénard convection: A T-RANS study. *J. Turbulence* **1**(8) (2000) 1–22.
17. Krettenauer, K. and Schumann, U., Numerical simulation of turbulent convection over wavy terrain. *J. Fluid Mech.* **237** (1992) 261–299.